Journal of Materials Chemistry A

Accepted Manuscript

ROYAL SOCIETY OF CHEMISTRY

www.rsc.org/materialsA

Enhancing the Crystallization and Optimizing Orientation of Perovskites Film via Controlling Nucleation Dynamics

Qiuju Liang, Jiangang Liu, Zhongkai Cheng, Yan Li, Liang Chen, Rui Zhang, Jidong Zhang and Yanchun Han*

State Key Laboratory of Polymer Physics and Chemistry, Changchun Institute of Applied Chemistry, Chinese Academy of Sciences, 5625 Renmin Street, Changchun 130022, P. R. China;

University of the Chinese Academy of Sciences, No.19A Yuquan Road, Beijing 100049, P. R. China.

Tel: 86-431-85262120, Fax: 86-431-85262120, Email: ychan@ciac.ac.cn

* To whom correspondence should be addressed

Abstract

The morphology of active layer is at the heart of perovskite solar cells. It is deeply related to charge transport and extraction, which depend on coverage ratio, crystallinity, crystal size and perhaps crystal orientation. However, the crystallization process in solution-processed perovskite film is ungovernable and there is no clear guideline for how to improve the film morphology. Here, we employed selective solvent annealing (SSA) method to control crystallization kinetics, producing a flat $CH_3NH_3PbI_xCl_{3-x}$ film with almost full coverage, micron scale grain size, enhanced crystallinity and optimized crystal orientation. The improved morphology is attributed to the formation of uniformly distributed nucleus of perovskite before thermal annealing, resulting from the selective solubility of selective solvent, which accelerates the crystallization of lead iodide (PbI_2) and the intercalation of

methylammonium iodide (MAI) into PbI_2 crystal lattice. Furthermore, driven by thermodynamics, the nucleus tend to rearrange during the thermal annealing process, thus the crystal orientation turns from (*h k* 0) (*h* = *k*) to (*h* 0 0) orientation, which lead to the corner of the inorganic framework contact with the substrate. The enhanced crystallinity, enlarged crystal size and optimized crystal orientation are beneficial for the carrier collection due to the prolonged carrier life time and reduced carrier recombination, which resulted in the highest power conversion efficiency (PCE) of 12.38%, about 37% increase compared with the reference device.

Introduction

Low fabrication cost, ease of processing (solution processing), and excellent light-harvesting characteristics make perovskite material currently among the most competitive candidates for thin-film photovoltaic (PV) applications.[1] Since the organometal halide perovskites were first used as sensitizers in solar cells, solution-processed hybrid perovskite solar cells have now achieved remarkably high photovoltaic power conversion efficiency of 20.1%, which have already reached the commercial requirement of high efficiency.[2-5]

As well known, the morphology of perovskite film is very crucial to device performance.[6-8] However, solution-processed films usually suffer from low film coverage ratio, small grain size and low crystallinity due to the uncontrollable crystallization process which are detrimental to device performance, such as light absorption, carrier transport and collection.[9-12] It is recently reported that the crystallization process is sensitive to interfacial energy, solvent choice and deposition temperature et al. Therefore, controlling nucleation and crystallization process during film deposition and annealing is an attractive route to improve perovskite film morphology.[13-15] Cheng et al. reported an effective way to promote the nucleation via spin-coating poor solvent onto perovskite wet films to improve the perovskite film morphology. The poor solvent would extract the main solvent and condense the solution on the substrate, which impelled the precursor solutes to nucleate, forming a highly uniform film with enhanced crystallinity.[16] Similarly, the introduction of chloridion could also facilitate the nucleation process, which functioned as heterogeneous nucleation sites and enhanced the nucleus density of the perovskite film, resulting in a perfect morphology.[14,17,18] In addition, regulating the crystals growth process could also improve the film morphology. Adding solvents with coordination effect with lead ions into the precursor solution could slow down the crystallization process due to the formation of "coordinated intermediate phase", which encouraged homogenous nucleation and obtained a continuous perovskite film.[19,20] Using good solvent to treat perovskite film during the thermal annealing

process is also an effective method.[21] It promoted the diffusion of precursors during the crystal growth which resulted in a large perovskite grain size.

Besides film quality, the crystal orientation may also has profound influence on device performance. As we know, perovskite is a typical kind of organic-inorganic hybrid material, in which an extended framework formed by the iodide ions (I^-) and lead ions (Pb^{2+}) by strong ionic or covalent interactions, while the organic component intercalates into the framework through Van der Waals forces.[22] Thus, there are many types of contact between the perovskite and substrate interface. For the (100) direction, the corner of the inorganic framework would contact at the perovskite/substrate interface, while for the (110) direction, the inorganic framework represents the edge contact at the interface. The different contact at the interface may affect the charge extraction and collection. However, as far as we know, perovskite crystals processed by solution-processing technique usually exhibit strong (*h k 0*) (*h* = *k*) preferred orientation.

In this manuscript, we develop a simple and effective strategy, selective solvent annealing (SSA), to optimize the morphology and orientation of $CH_3NH_3PbI_{3-x}Cl_x$ film by controlling the nucleation process. Selective solvent, isopropanol (IPA), acts as good solvent for MAI but poor solvent for PbX_2 (X=Cl or I). The selective solubility results in a high degree of supersaturation of Pb^{2+} and X^-, thus favoring the precipitation and crystallization of lead halide. Meanwhile, IPA forms H-bonding with MAI, which could assist the intercalation of MA^+ into the lead halide crystal lattice, ultimately forming uniform and dense perovskite crystals nucleus. The formation of nucleus would avoid slow nucleation process, resulting in flat perovskite films with enlarged grain size and enhanced crystallinity. In addition, the nucleus tend to rearrange via Ostwald ripening process to attain thermodynamic stability during thermal annealing process, promoting the crystal orientation to transform into (*h* 0 0) orientation. The improved film morphology and orientation would facilitate the carrier collection due to the prolonged carrier life time and reduced carrier recombination, leading to a remarkable increasement of device performance.

Experimental

Materials

Methylammonium iodide (MAI) and lead chloride ($PbCl_2$) were purchased from Yingkou Optimal Choice Trade, China. [6, 6]-phenyl-C61-buryric acid methyl was purchased from American Dye Source. The bis-functional of C70 (C70-bis) was purchased from 1-Material, Canada. N, N-dimethylformamide (DMF) was purchased from Adrich company. Isopropanol (IPA), toluene (TOL) were purchased from Beijing Chemical Factory, China. The materials were used without further purification.

The solvent vapor annealing

During the solvent vapor annealing process, the active layer was placed into a glass tube which contained toluene, isopropanol and DMF at bottom, respectively. Stable vapor gradient along the tube could be obtained after 15min since liquid solvent location was fixed. The vapor pressure of sample was $P = 0.54$ (25 °C) (The length of tube is 3 cm and the liquid height is 0.2 cm. The solvent vapor pressure P is given by $P = L/L_0$, where L is the distance from the up edge of the setup to the specimen position and L_0 is the length given by distance from the up edge of the setup to the surface of the solvent at the bottom of the tube). The samples of toluene, isopropanol and DMF were treated under this vapor pressure for 180s, 120s and 20s respectively as active layer spin-coated.

Fabrication of thin-film perovskite solar cells

The devices were fabricated in the configuration of indium tin oxide (ITO)/PEDOT:PSS/$CH_3NH_3PbI_{3-x}Cl_x$/[6,6]-phenyl-C61-butyric acid methyl ester (PC61BM)/fullerene surfactant (C70-bis)/Al. The ITO glass substrates were cleaned sequentially with detergent and deionized water, acetone, and isopropanol under sonication for 10min. After drying by nitrogen flow, substrates were treated with UV-ozone for 25 min. Poly (ethylenedioxythiophene): poly (styrenesulfonate) (PEDOT:PSS, Baytron P4083, filtered through a 0.45 μm nylon filter) layer was first spin-coated at 5k rpm for 40 s on this well-cleaned ITO glass and dried at 140 °C in

vacuum for 30 min. The substrates were transferred into a N_2-filled glovebox, where the thin-film perovskite layers were spin-coated from a homogeneous 30 wt% ($PbCl_2$:MAI with a molar ratio of 1:3 in DMF) precursor solution at 7k rpm for 45 s (300nm thickness) on the hot substrates (about 63 °C) and then annealed at 75 °C for 5 h. Afterward, the $PC_{61}BM$ (15 mg/mL in chloroform) and C70-bis surfactant (2 mg/mL in isopropyl alcohol) were then sequentially deposited by spin coating at 3k rpm for 60 s, respectively. Finally, a layer structure of Al (90 nm) was deposited at top of the active layer by thermal evaporation in a vacuum of 2×10^{-4} Pa to complete the device fabrication.

Characterization

The morphology of hybrid perovskite films was acquired by field-emission scanning electron microscopy (FESEM) using a Micro FEI Philips XL -30-ESEMFEG microscope at an accelerating voltage of 20 kV. The sample were sputter coated with gold before SEM observation. The elements distribution of film was analyzed using an energy dispersive spectroscopy (EDS, GENESIE 2000-EDAX).

The crystallinity of perovkite film was analyzed using out-of-plane grazing incidence X-ray diffraction (GIXD) measurements, two-dimentional GIXD (2D GIXD). The GIXD profiles were obtained by using a Bruker D8 Discover reflector with an X-ray generation power of 40 kV tube voltage and 40 mA tube current. The measurements were achieved in a scanning interval of 2θ between 3 and 60°. The 2D GIXD profiles were obtained by using a Rigaku Smartlab instrument with an X-ray generation power of 40 kV tube voltage and 30 mA tube current and BL14B1 at Shanghai Synchrontron Radiation Facility (SSRF; λ=0.124 nm).

The photon absorption of active layer and situ absorption spectrum were recorded by combining UV-vis absorption spectroscopy (Shimadzu UV 3600 spectrophotometer at a spectral range of 300-1000 nm) with a home-made heater.

To demonstrate the orientation evolution, situ 2D GIXD was operated through combining Rigaku SmartLab instrument with an X-ray generation power of 40 kV

tube voltage and 30 mA tube current with a home-made heater. The perovskite film without solvent vapor treatment was annealed at 65°C and the film with solvent vapor treatment was annealed at 75 °C under vacuum.

Current density-voltage (*I-V*) characteristics of the PV cells were measured using a computer controlled Keithley 236 source meter under AM1.5G illumination from a calibrated solar simulator with irradiation intensity of 100 mW/cm^2. The device area was 12 mm^2, determined by the overlap of the cathode and anode. An aperture size of 10.6 was used to define the light absorption area, which would avoid the overestimation of the photocurrent density by the optical pining effect.[23]

Nanosecond fluorescence lifetime experiments were performed using the time-correlated single-photon counting (TCSPC) system under right-angle sample geometry. A 400 nm picosecond diode laser (Edinburgh Instruments EPL375, repetition rate 20 MHz) was used to excite the samples. The fluorescence was collected by a photomultiplier tube (Hamamatsu H5783p) connected to a TCSPC board (Becker & Hickl SPC-130). The time constant of the instrument response function (IRF) is about 220 ps.

Results and discussion

The selective solvent (IPA) annealing (SSA) was employed to improve the morphology and orientation of perovskite films. Due to the accelerated nucleation dynamic during SSA process and the crystal fusion during thermal annealing process, a uniform and high crystallized perovskite film with (*h* 0 0) orientation was obtained, which is beneficial for the device performance.

Increasing the film coverage and grain size by regulating the nucleation and crystal growth process

Recently, it has been reported that the uncontrollable nucleation kinetics usually leads to poor morphology of perovskite film fabricated by solution-processing technique.[19,24,25] Here, we employed SSA method to control the nucleation and crystal

growth kinetics, finally obtained a continuous film with large grain size and enhanced crystallinity.

Fig. 1 shows the scanning electron microscope (SEM) images of pristine film and film treated by SSA (treated film). As we can see, the pristine film contains many pin-holes and the crystal size is less than 200 nm as shown in Fig. 1 (A) and (a), which is caused by the high boiling point (153 °C) and slow evaporation of DMF.[15] While the treated film exhibits almost full surface coverage with micron-sized grains, which pack in a dense manner as shown in Fig. 1 (B) and (b) (the optimization of different annealing time are shown in Fig. S1).

The improved film morphology could be attributed to the regulated nucleation process due to the SSA treatment. In order to testify the effects of IPA vapor on the nucleation process, we vacuumized the films treated by IPA vapor for different times immediately to freeze its morphology. As shown in Fig. 2, the as spin-coated film without annealing (0 s) is a uniform flat film, and it was composed by lead halide and the coordinated Pb^{2+}-N, N-dimethylformamide (DMF) compound, which can be confirmed by XRD (Fig. S2 A).[20] While some distinct changes were gradually observed with the extended annealing time: at first, small regular cubes appear and its number increase gradually (30 s~120 s), the cubes are perovskite crystals as confirmed by XRD as shown in Fig. S2 (A); subsequently, the cubes get bigger and some spherical aggregates appear on the top of the film (150 s~210 s), which are formed by MAI deduced by energy dispersive spectroscopy (EDS) results (Fig. S2 B). Based on these phenomena mentioned above, we supposed the changes stem from the special function of IPA. First, due to the low solubility to lead halide, IPA would inhibit the coordination between Pb^{2+} and DMF molecules and promote the crystallization of lead halide. In addition, H-bonding could be formed between MA^+ and IPA, which promotes the intercalation of MA^+ into lead halide to form perovskite nucleus owning to the small molecular size and ease of volatilization of IPA. If the film was over exposed to IPA vapor (> 150 s), MAI would form large aggregates. The aggregates inhibited the MA^+ intercalating into inorganic framework, and led to an

incomplete coverage morphology as shown in Fig. S1. To sum up, the proper annealing time is 120 s, which could promote the formation of uniform and dense perovskite nucleus, a precondition to form continuous film.

To further explore the underlying nucleation crystal growth kinetics mechanism, time dependence of UV-vis absorption spectra (In-situ UV-vis absorption spectra) during thermal annealing process was conducted (shown in Fig. 3). Compared with the spectrum of the pristine film (Fig. 3A), the spectrum of treated film (Fig. 3B) is broaden and its eventual absorption intensity is stronger, which means an enhanced crystallinity of perovskite after the SSA. In order to quantify the change of crystallization process during thermal annealing treatment, we tracked the peak intensity variances at 730 nm ($I_{increase}$) against the time (t), of which the absorbance is correspond to the amount and size of perovskite crystals in films.[26] As shown in Fig. 3(a), the crystallization starts from a relatively slow nucleation process (0 – 112 min), followed by a rapid growth process (112 – 256 min), and their corresponding rates are k_{pn} = 2.8 E^{-4} and k_{pc} = 1.25 E^{-3}, respectively.[14] For treated film, the whole crystallization process is shorten to 128 min as shown in Fig. 3(b). Its nucleation process last about 72 min (k_{pn} = 0) and crystal growth process last about 50 min (k_{sc} = 3.0 E^{-3}), which are faster than pristine film. It is worth noticeable that the k_{pn} for treated film is 0 and the absorption intensity for nucleus is about 0.09 (the corresponding absorption intensity for pristine film is 0.05). It means that a mass of nucleus have already formed during the SSA process, which is an important precondition for forming uniform perovskite film. Due to the existed nucleus, it would avoid the gradual formation of nucleus during thermal annealing, which tends to result in a poor morphology of perovskite film.[27] In addition, the faster crystal growth rate of treated film indicates the formed nucleus favors the crystal growth. The faster transition of the perovskite reduces the processing time which makes it easier for fabrication as well as save the energy during the manufacture of solar cells.

The optimized crystal orientation resulting from crystal growth kinetics

In order to get further insight into crystal structure, the out of plane X-ray diffraction (XRD) was performed. As shown in Fig. 4, two obvious peaks are found at 14.08° and 28.5°, which can be assigned to the (110) and (220) crystal planes of the hybrid perovskite orthorhombic lattice. While for the treated film, except the (*h k* 0) (*h* = *k*) diffraction signals, the peaks located at 31.9°, 40.7°, and 43.3° corresponding to (310), (224) and (314) diffraction signals are also obvious. The appearance of these diffraction signals indicated that the orientation of perovskite crystals must be changed after the SSA treatment.

In order to probe the orientations of perovskite crystals, two-dimentional GIXD (2D-GIXD) was performed. As shown in Fig. 5(A), 2D-GIXD result for pristine film exhibits concentrated"spotty" pattern along the q_z axis at azimuthal angle 90° (the scattering signals at q = 10 nm^{-1} is assigned to the (110) plane of perovskite structure[28]), signifying that (*h k 0*) (*h* = *k*) are highly oriented in the out-of-plane direction (the schematic diagram is shown in Fig. 5E). Nevertheless, the spotty pattern for treated film split into several points and their azimuthal angle distributed at 22.5°, 45°, 66.5° and 90°, respectively. According to the dihedral angel relationship (shown in S5), when the (*h k* 0) (*h* = *k*) signal centered at 45°, its (*h* 0 0) lattice planes must be perpendicular to the substrate as shown in Fig. 5(F). To quantify the amount of crystals that adopt different orientations, we calculated the two-dimensional signal intensity according to azimuthal angle (Fig. 5C corresponds to Fig. 5A and the Fig. 5D corresponds to Fig. 5B). The area under the azimuthal curve is in proportion to the crystallinity of perovskite film. As a result, we could compare the number of crystals adopted different orientations. Here, the whole relative crystallinity degree of pristine film is 49259 ($A1_{0\text{-}90}$ = 49259) and the one of treated film is 59269 ($A2_{0\text{-}90}$ = 59269), which implies enhanced crystallinity of perovskite after the SSA treatment. Furthermore, the ratio of crystals adopted (*h* 0 0) orientation ($A1_{35\text{-}55}/A1_{0\text{-}90}$) for pristine film is 12.7%. While the corresponding ratio ($A2_{35\text{-}55}/A2_{0\text{-}90}$) increased to 26.3% after the SSA treatment. These changes suggest that the SSA treatment promoted the crystals to adopt (*h* 0 0) orientation. According to the perovskite crystal

structure, the crystals adopted (*h* 0 0) orientation, i.e. the corner of the inorganic framework would contact between the perovskite and substrate interface, which may be beneficial for carrier transportation and collection due to higher carrier mobility. [29,30] As far as we know, it is the first time to adjust the orientation of perovskite, which is meaningful to understand the fundamental crystal structure.

To probe the evolution of perovskite orientation, we employed In-situ smart with 2D detection capability (In-situ 2D-GIXD). As shown in Fig. 6(A), three diffraction signals for the pristine film were observed before thermal annealing. Combining the 2D-smart with Rigaku 2D Data Processing software, these three signals are assigned to 11.0°, 12.2° and 16.5° (Fig. S6), which are the diffraction signals of lead halide.[22,27] After thermal annealing, the signal intensity of lead halide became weak, while the signal corresponding to $CH_3NH_3PbI_{3-x}Cl_x$ (14.2°) appeared (84 min) and its intensity became stronger gradually (84 – 224 min). It implies the film underwent a complete transition from lead halide to perovskite. Moreover, the signal of perovskite is also distributed along the q_z axis, which suggests the (*h k 0*) (*h* = *k*) crystal plane is highly oriented in the out-of-plane direction. However, the transition process for treated film is different as shown in Fig. 6(B). At the beginning, not only the lead halide signal but also the perovskite signal could be observed. Moreover, the signal of lead halide was weak while the signal of perovskite was relative strong, and all of them were distributed around q_z axis. Both of these demonstrate that the SSA treatment could promote the formation of perovskite nucleus, which consists with the XRD as shown in Fig. S2. During the thermal annealing process, lead halide transformed into perovskites gradually. Surprisingly, in addition to azimuth angle of 90°, the signal of perovskite also appeared around azimuth angle of 45° (42 min) and its intensity became stronger. This phenomenon indicates that some of the formed perovskite rearranged and adopted (*h* 0 0) orientation during thermal annealing process. This dynamic change about crystal orientation of perovskite is a novel observation and may be useful to understand the perovskite formation dynamics.

From the results we get above, mechanism of optimizing film morphology and orientation via SSA treatment can be concluded as followings (as shown in schematic diagram 1): During SSA process, IPA promotes the precipitation and crystallization of lead halide (as shown in Fig. S8) because it has a low solubility to lead halide. Furthermore, IPA assists the diffusion of MA^+ and I^- since it acts good solvent for MAI and forms H-bonding with MA^+, thus promotes the intercalation of MA^+ into inorganic framework, resulting in formation of uniform perovskite crystal nucleus. During thermal annealing process, the nucleus would rearrange and coalesce via Ostwald ripening process to attain thermodynamic stability owing to the surface energy minimization, which results in an increased crystal growth rate and optimized crystal orientation.

Enhanced photoabsorption and carrier extraction efficiency

As is well known, the morphology of perovskite film has profound influence on device performance. Here, we improved the crystallinity, coverage as well as orientation of perovskite film, which resulted in an increased light harvesting, longer carrier lifetime and higher carrier extraction efficiency.

The device parameters for pristine film and treated film were extracted from the reverse and forward current-voltage (*J-V*) curves under simulated AM1.5, 100 mW/cm^2 sunlight (as shown in Fig. 7).[31] The device based on pristine perovskite film exhibits reverse short-circuit current density (J_{SC}), open-circuit voltage (V_{OC}) and fill factor (*FF*) of 14.83 mA cm^{-2}, 0.91 V and 0.67, respectively, with a low power conversion efficiency (PCE) of 9.04%. While the performance of device based on treated film increased to 12.38%, with improved reverse J_{SC}, V_{OC} and *FF* of 17.85 mA/cm^2, 0.95 V, and 0.73, respectively. The forward *J-V* curves for device with and without SSA treatment were also conducted, and its corresponding parameters were listed in Table 1. There is no big discrepancy between the reverse and forward device parameters, indicating the reliability of *J-V* curve measurement. After SSA treatment, the higher V_{OC} could be ascribed to the well-developed crystals and optimized crystal orientation, which reduce the energy losses during the carrier transport process. The

increasement of J_{SC} is mainly attributed to the enhanced absorption, arising from the enhanced crystallinity and increased film coverage. In addition, the increased J_{SC} is in good agreement with external quantum efficiency (EQE) measurement (Fig. 7B), which have an error range of 2%. Moreover, the device with SSA treatment also shows a higher *FF*, which implies a reduced recombination during the charge transport process.

In order to confirm our viewpoint, the internal quantum efficiency (IQE) is calculated. Assuming all of the light transmitted through ITO/glass was absorbed by perovskite film, the IQE was calculated by dividing the EQE with the transmittance (Fig. S12).[24,31] The device fabricated by treated film exhibits a higher IQE over the whole spectrum, which indicates the photogenerated carriers are collected at the electrodes with few losses. The increased IQE must be caused by enhanced crystallinity, grain size and optimization of crystal orientation. Due to a higher crystallinity and large crystals, the number of defects and grain boundary is reduced, leading to fewer trapped free carriers.[8] Moreover, the optimized orientation with inorganic framework perpendicular to the substrate would further decrease the barrier energy of charge transport, which is benefial to the charge extraction.

The reduced recombination of carriers was also reflected by its prolonged lifetime. Fig. 8 shows the femtosecond transient absorption (fs-TA) spectroscopy on the pristine film and treated film. In our experiment, the decay kinetics of TA signal for the perovskite films monitored at wavelength of 750 nm, extracted from the perovskite films prepared on the glass substrate. As we can see, there are two photobleaching (PB) negative peaks around 475 nm and 750 nm and the photoabsorption (PA) peak at 500-700 nm, which is consisted with previous reports.[32] The fs-TA spectra of the treated film shows stronger PB intensity, which means the number of photogenerated carriers is much bigger than the one in pristine film. This is also in line with the enhanced photoabsorption as shown UV-vis absorption spectrum, indicating an intense absorption of the perovskite excited states due to the enhanced crystallinity. To illustrate the charge recombination and transport properties, the decay

kinetics of the TA signal for the pristine film and treated film were employed (Fig. 8C). Asufit fits were performed to quantify the carrier kinetics. According to Asufit, the curve obtained from pristine film is fitted with two time constants, fast component (39 ps) and slow component (180 ps). According to previous reports,[33-35] the fast decay component might result from grain boundaries within the perovskite film, which could trap charge carriers. The long decay component could be attributed to recombination of free carriers in the radiative channel. After the SSA, the sample only exhibited a slow decay component. The absence of fast decay component may be originated from enhanced crystallinity and enlarged crystal size, which reduced the number of grain boundary, consequently, reducing the number of trapped charge carriers. Moreover, the slow decay component was prolonged to 335 ps, which is almost twice than the one in pristine film. This prolonged slow decay component might result from the improved morphology: enhanced crystallization and optimized orientation, which retarded recombination of free carriers, representing a longer carrier lifetime.

Conclusion

In summary, the nucleation kinetics and crystal growth of $CH_3NH_3PbI_{3-x}Cl_x$ hybrid perovskite were regulated by SSA method, producing a continuous film with enlarged grain size, enhanced crystallinity and optimized orientation. The improved film morphology is mainly attributed the formation of uniform perovskite nucleus and fast crystal growth caused by SSA process. In SSA process, IPA would promote the crystallization of lead halide and the intercalation of MAI due to the selective solubility, leading to the formation of uniformly distributed perovskite nucleus. The formation of the nucleus avoids the slow and inconformity of nucleation process in traditional film fabrication and favors crystal growth process, resulting in improved film coverage, enlarged grain size and enhanced crystallinity. Furthermore, the formed nucleus would rearrange via Ostwald ripening during thermal annealing process, resulting in the crystal adopting (*h* 0 0) orientation to attain thermodynamic

stability. The improved film coverage, enlarged crystal size, enhanced crystallinity and optimized crystal orientation are beneficial for the carrier collection due to the prolonged carrier life time and reduced carrier recombination, which resulted in an improvement of PCE from 9.04% to 12.38%, about 37% increase compared with the reference device.

Acknowledgment

This work was supported by the National Basic Research Program of China (973 Program-2014CB643505), the Strategic Priority Research Program of the Chinese Academy of Science (Grant No. XDB12020300). We also thank the Shanghai Synchrontron Radiation Facility (SSRF) for 2D GIXD measurement.

Figure captions

Table 1 Parameters of the device performance based on pristine and treated perovskite film under 100 mW cm^{-2} simulated AM1.5G illumination.

Schematic diagram 1 The schematic diagram of nucleation process during SSA process and crystal growth during thermal annealing process.

Fig. 1 Low-magnification and high-magnification SEM top-view images of perovskite film with and without SSA treatment: (A) and (a) without SSA treatment; (B) and (b) film with SSA treatment. All the films are thermal annealed 5 h at 75 °C.

Fig. 2 SEM top-view images of perovskite film with SSA treatment for different times. All the films were placed under vacuum 2 hours without thermal annealing.

Fig. 3 The situ UV-vis absorption spectra of perovskite film without (A) and with (B) SSA treatment; The evolution of absorption intensity at 730 nm of the perovskite film without (a) and with (b) SSA treatment. All the films to be thermal annealed were heated at 75 °C under flowing nitrogen.

Fig. 4 The out of plane XRD profile shows the crystallinity of pristine and treated perovskite film.

Fig. 5 The 2D-GIXD patterns of pristine (A) and treated (B) perovskite films. Azimuthal line scans for (110) peak of the pristine (C) and treated (D) perovskite films. The schematic diagram of the crystals adopted (*h k* 0) (*h* = *k*) orientation (E) and (*h* 0 0) orientation (F).

Fig. 6 The In-stiu 2D-GIXD patterns for pristine (A) and treated (B) perovskite film. All the films to be thermal annealed were heated at 75 °C.

Fig. 7 The *J-V* curve for the devices based on pristine (A) and treated (B) perovskite film, the forward (short circuit → open circuit) and reverse (open circuit → short circuit) scans with 10 mV voltage steps under 100 mW cm^{-2} simulated AM1.5G illumination. (C) The EQE and IQE plot of devices based on pristine and treated perovskite film.

Fig. 8 (A) Transient-absorption spectra at several delay times following excitation at 400 nm for pristine (A) and treated (B) perovskite films. (C) The transient decay

dynamics of pristine and treated perovskite film, the pump wavelength is 750 nm.

Table 1.

	Voc (V)	*Jsc* (mA/cm2)	*FF*	*PCE* (%)
Pristine film reverse	**0.92**	**14.68**	**0.67**	**9.04**
Pristine film forward	**0.91**	**14.81**	**0.66**	**8.89**
Treated film reverse	**0.95**	**17.85**	**0.73**	**12.38**
Treated film forward	**0.95**	**17.84**	**0.73**	**12.37**

Schematic diagram 1.

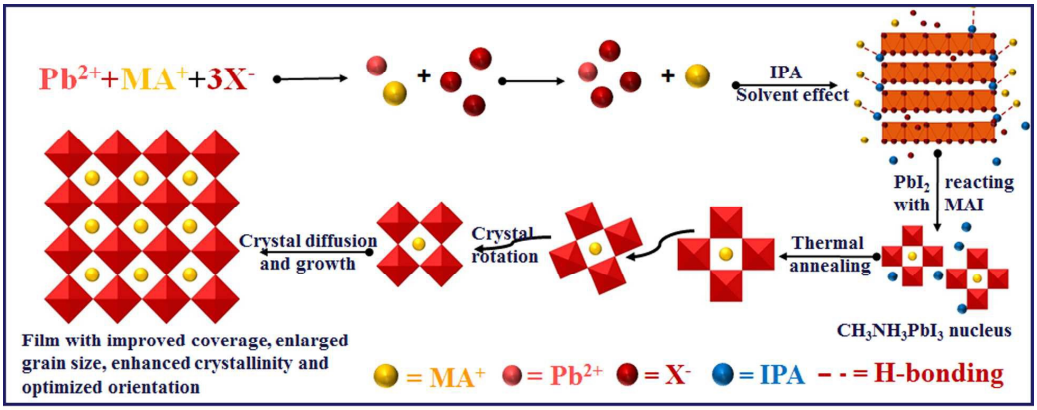

Figure 1.

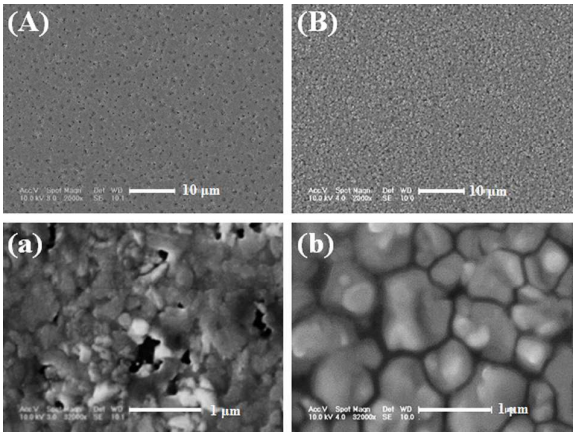

Figure 2.

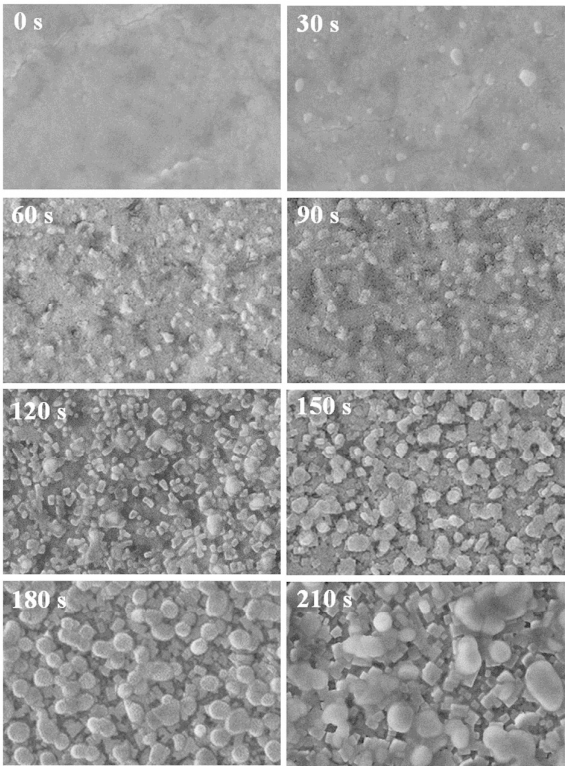

Figure 3.

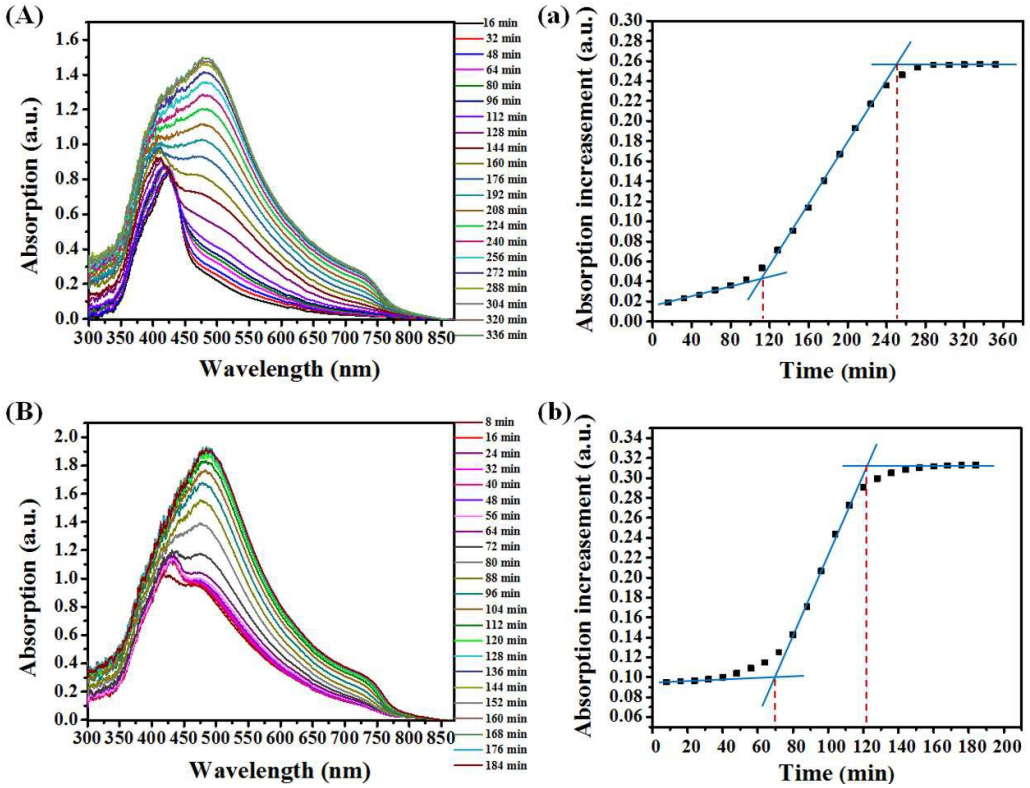

Figure 4.

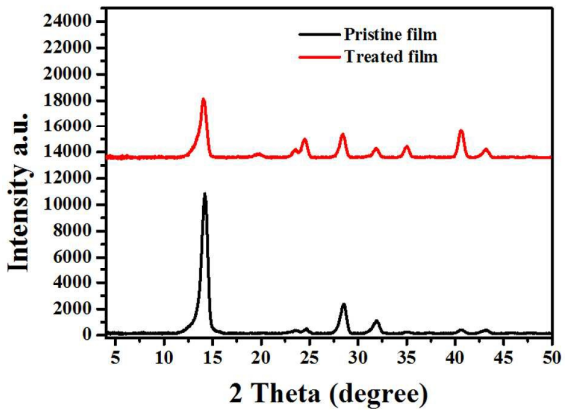

Figure 5.

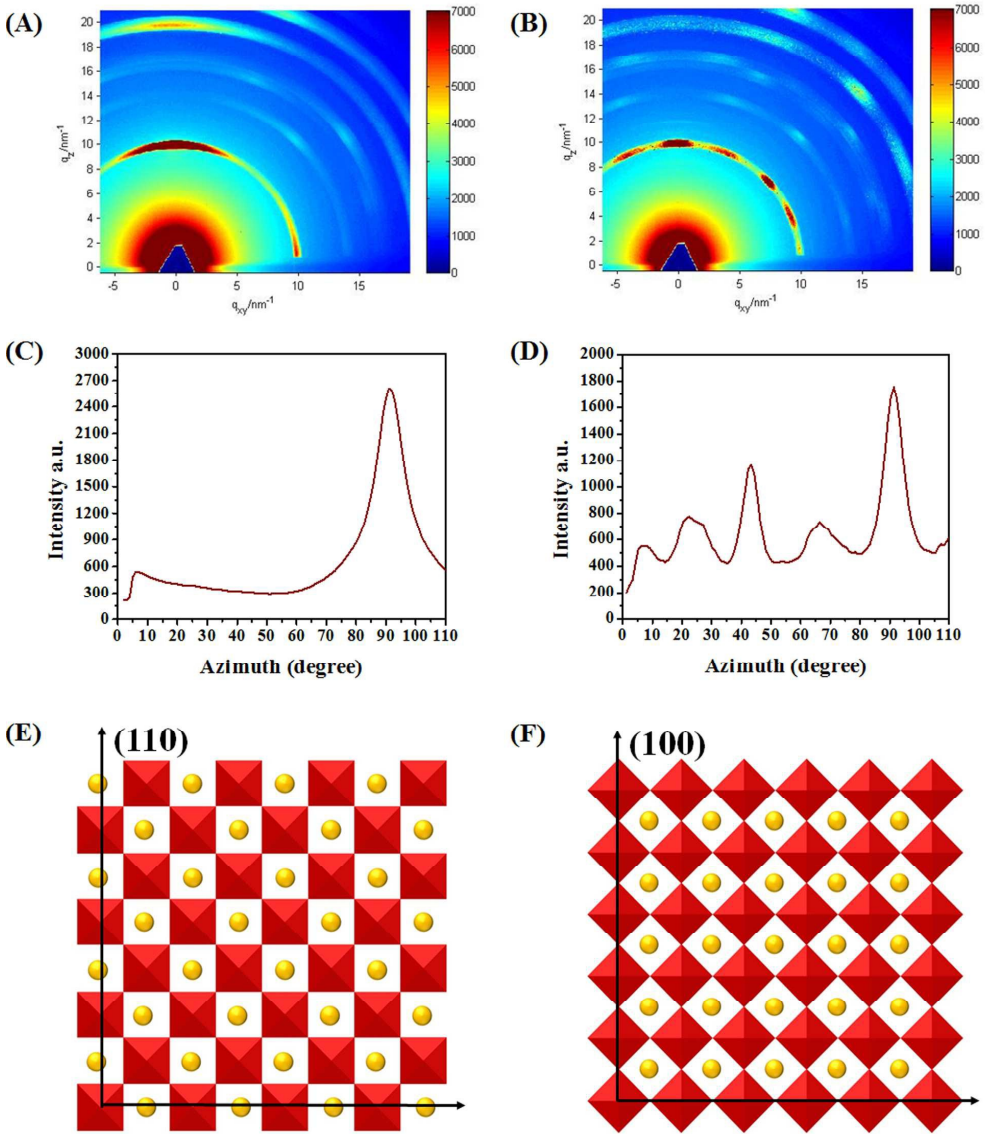

Figure 6.

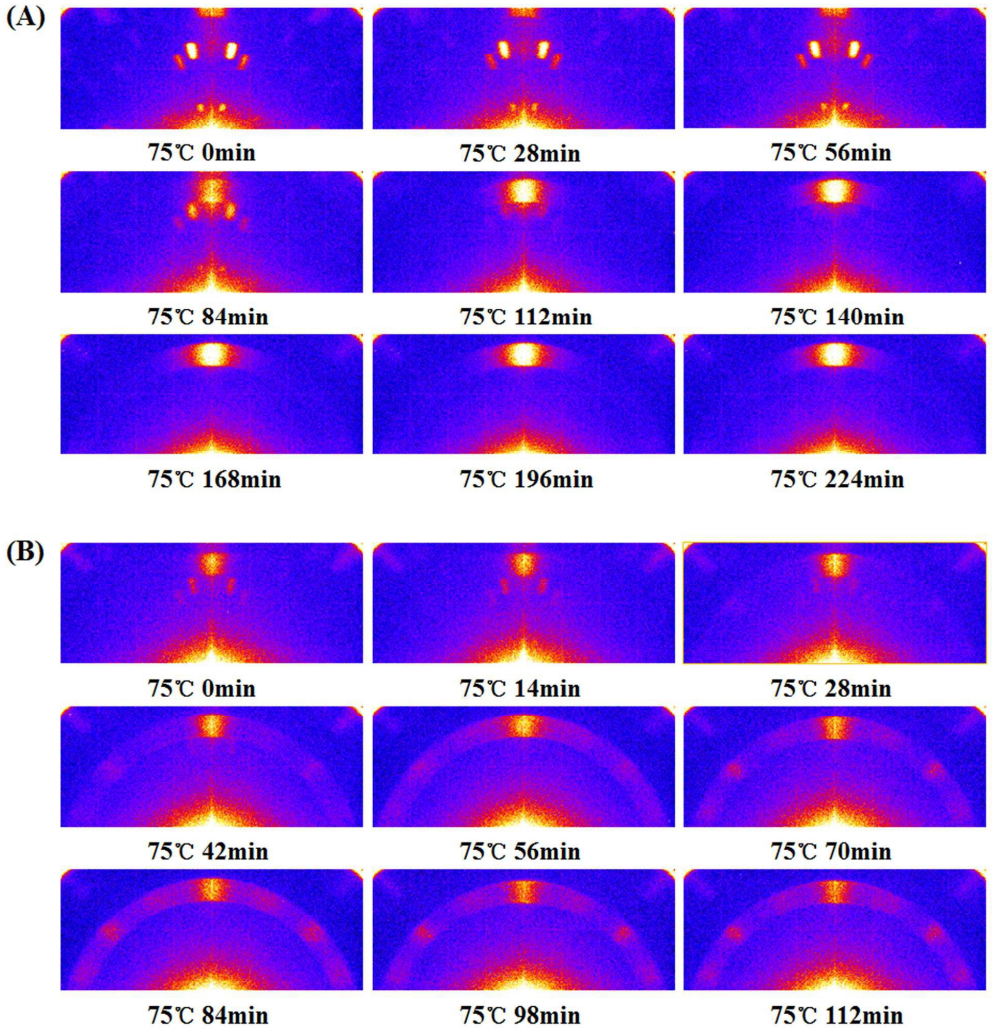

Figure 7.

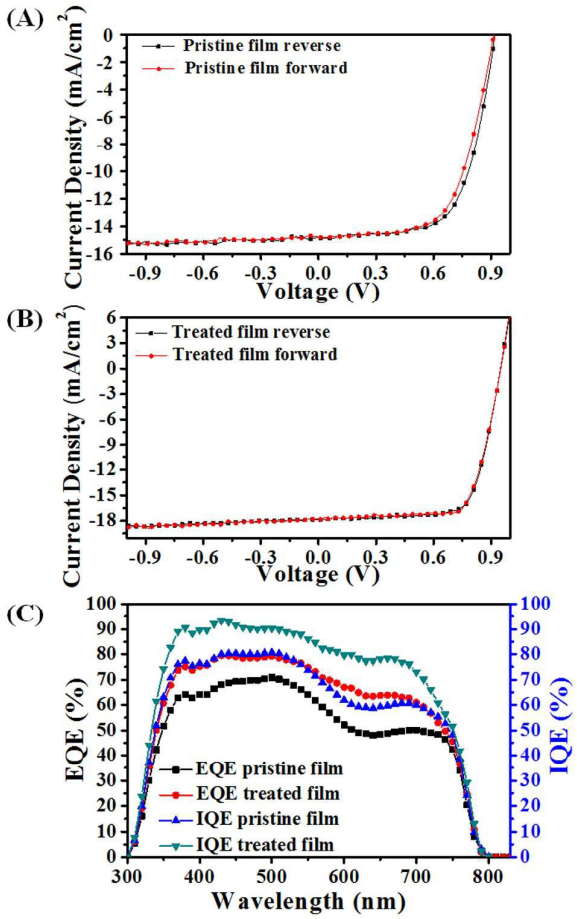

Figure 8.

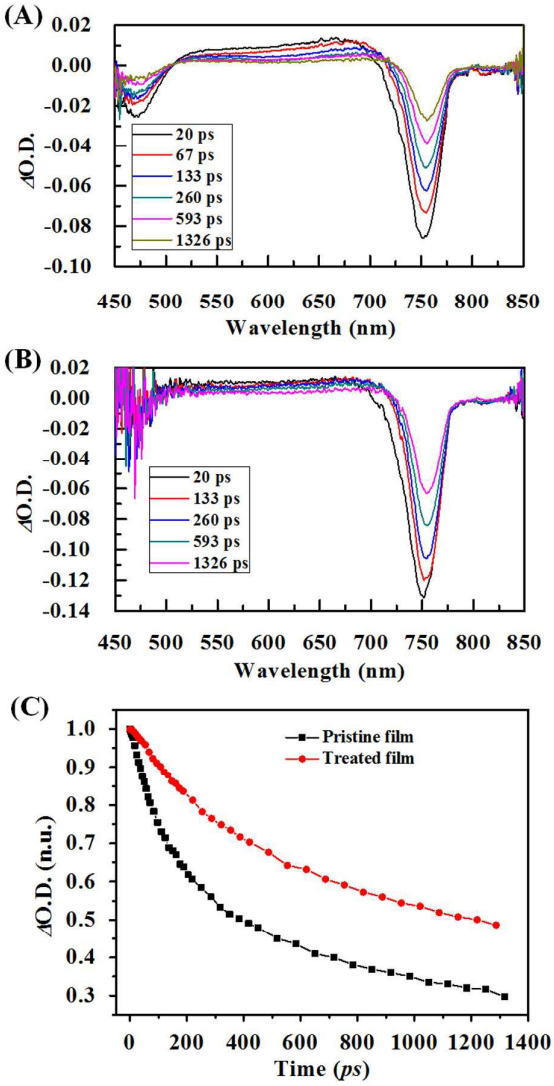

References

1. L. Zuo, Z. Gu, T. Ye, W. Fu, G. Wu, H. Li and H. Chen, *J. Am. Chem. Soc.*, 2015, **137**, 2674-2679.
2. A. Kojima, K. Teshima, Y. Shirai and T. Miyasaka, *J. Am. Chem. Soc.*, 2009, **131**, 6050-6051.
3. H. Zhou, Q. Chen, G. Li, S. Luo, T.-B. Song, H.-S. Duan, Z. Hong, J. You, Y. Liu and Y. Yang, *Science*, 2014, **345**, 542-546.
4. J.-W. Lee, T.-Y. Lee, P. J. Yoo, M. Gratzel, S. Mhaisalkar and N.-G. Park, J. Mater. Chem. A, 2014, **2**, 9251–9259.
5. W. S. Yang, J. H. Noh, N. J. Jeon, Y. C. Kim, S. Ryu, J. Seo, S. I. Seok, *Science*, 2015, **348**, 1234-1237.
6. L. Wang, W. Fu, Z. Gu, C. Fan, X. Yang, H. Li and H. Chen, *J. Mater. Chem. C*, 2014, **2**, 9087-9090.
7. W. Nie, H. Tsai, R. Asadpour, J.-C. Blancon, A. J. Neukirch, G. Gupta, J. J. Crochet, M. Chhowalla, S. Tretiak, M. A. Alam, H.-L. Wang and A. D. Mohite, *Science*, 2015, **347**, 522-525.
8. Q. Chen, H. Zhou, Z. Hong, S. Luo, H.-S. Duan, H.-H. Wang, Y. Liu, G. Li and Y. Yang, *J. Am. Chem. Soc.*, 2014, **136**, 622-625.
9. W. Zhang, M. Saliba, D. T. Moore, S. K. Pathak, M. T. Hörantner, T. Stergiopoulos, S. D. Stranks, G. E. Eperon, J. A. Alexander-Webber, A. Abate, A. Sadhanala, S. Yao, Y. Chen, R. H. Friend, L. A. Estroff, U. Wiesner and H. J. Snaith, *Nat Commun.*, 2015, DOI: 10.1038/ncomms7142.
10. H. Wang, Y. He, Y. Li and H. Su, *J. Phys. Chem. A*, 2012, **116**, 255–262.
11. Q. Dong, Y. Fang, Y. Shao, P. Mulligan, J. Qiu, L. Cao and J. Huang, *Science*, 2015, **347**, 967-969.
12. D. Shi, V. Adinolfi, R. Comin, M. Yuan, E. Alarousu, A. Buin, Y. Chen, S. Hoogland, A. Rothenberger, K. Katsiev, Y. Losovyj, X. Zhang, P. A. Dowben, O.F. Mohammed, E. H. Sargent and O. M. Bakr, *Science*, 2015, **347**, 519-522.
13. N. J. Jeon, J. H. Noh, Y. C. Kim,W. S. Yang, S. Ryu1 and and S. I. Seok, *Nat. Mater.*, 2014, **13**, 897-903.
14. Y. Tidhar, E. Edri, H. Weissman, D. Zohar, G. Hodes, D. Cahen, B. Rybtchinski and Saar Kirmayer, *J. Am. Chem. Soc.*, 2014, **136**, 13249-13256.
15. M. Saliba, K. W. Tan, H. Sai, D. T. Moore, T. Scott, W. Zhang, L. A. Estroff, U. Wiesner and H. J. Snaith, *J. Phys. Chem. C*, 2014, **118**, 17171-17177.
16. M. Xiao, F. Huang, W. Huang, Y. Dkhissi, Y. Zhu, J. Etheridge, A. Gray-Weale, U. Bach, Y.-B. Cheng and L. Spiccia, *Angew. Chem. Int. Ed.*, 2014, **53**, 1-7.

17. S. T. Williams, F. Zuo, C.-C. Chueh, C.-Y. Liao, P.-W. Liang and A. K.-Y. Jen, *Acs Nano*, 2014, **8**, 10640-10654.

18. M. I. Dar, N. Arora, P. Gao, S. Ahmad, M. Grätzel and M. K. Nazeeruddin, *Nano Lett.*, 2014, **14**, 6991-6996.

19. Y. Wu, A. Islam, X. Yang, C. Qin, J. Liu, K. Zhang, W. Penga and L. Han, *Energy Environ. Sci.*, 2014, **7**, 2934-2938.

20. P.-W. Liang, C.-Y. Liao, C.-C. Chueh, F. Zuo, S. T. Williams, X.-K. Xin, J. Lin and A. K. Y. Jen, *Adv. Mater.*, 2014, **26**, 3748-3754.

21. Z. Xiao, Q. Dong, C. Bi , Y. Shao , Y. Yuan and J. Huang, *Adv. Mater.*, 2014, **26**, 6503-6509.

22. Y. Zhao and K. Zhu, *J. Am. Chem. Soc.*, 2014, **136**, 12241-12244.

23. E. Zimmermann, P. Ehrenreich, T. Pfadler. J. A. Dorman, J. Weickert and L. S-Mende, *Nat. Photonics*, 2014, **8**, 669-672.

24. T. Vetter, M. Iggland, D. R. Ochsenbein, F. S. Hänseler and M. Mazzotti, *Cryst. Growth Des.*, 2013, **13**, 4890-4905.

25. M. Xiao, F. Huang, W. Huang, Y. Dkhissi, Y. Zhu, J. Etheridge, A. Gray-Weale, U. Bach, Y.-B. Cheng and L. Spiccia, *Angew. Chem. Int. Ed.*, 2014, **126**, 10056-10061.

26. Y. Tidhar, E. Edri, H. Weissman, D. Zohar, G. Hodes, D. Cahen, B. Rybtchinski and S. Kirmayer, *J. Am. Chem. Soc.*, 2014, **136**, 13249-13256.

27. S. Ahmad, P. K. Kanaujia, W. Niu, J. J. Baumberg and G. Vijaya Prakash, *ACS Appl. Mater. Interfaces*, 2014, **6**, 10238-10247.

28. K. W. Tan, D. T. Moore, M. Saliba, H. Sai, L. A. Estroff, T. Hanrath, H. J. Snaith and U.Wiesner, *ACS Nano*, 2014, **8**, 4730-4739.

29. P. Gao, M. Grätzel and M. K. Nazeeruddin, *Energy Environ. Sci.*, 2014, **7**, 2448-2463.

30. A. Mei, X. Li, L. Liu, Z. Ku, T. Liu, Y. Rong, M. Xu, M. Hu, J. Chen, Y. Yang, M. Grätzel and H. Han, *Science*, 2014, **345**, 295-298.

31. C. Jeffrey A, M. Joseph S and K. Prashant V, *J. Phys. Chem. Lett*., 2015, **6**, 852−857.

32. J. Seo, S. Park, Y. C. Kim, N. J. Jeon, J. H. Noh, S. C. Yoon and S. I. Seok, *Energy Environ. Sci.*, 2014, **7**, 2642-2646.

33. L. Wang, C. McCleese, A. Kovalsky, Y. Zhao and C. Burda, *J. Am. Chem. Soc*., 2014, **136**, 12205-12208.

34. J. S. Manser and P. V. Kamat, *Nat. Photonics*, 2014, **8**, 737-743.

35. C. S. Ponseca, T. J. Savenije, M. Abdellah, K. Zheng, A. Yartsev, T. Pascher, T. Harlang, P. Chabera, T. Pullerits, A. Stepanov, J.-P. Wolf and V. Sundström, *J. Am. Chem. Soc.*,**136**, 5189-5192.

Enhancing the Crystallization and Optimizing Orientation of Perovskites Film via Controlling Nucleation Dynamics

Graphical Abstract

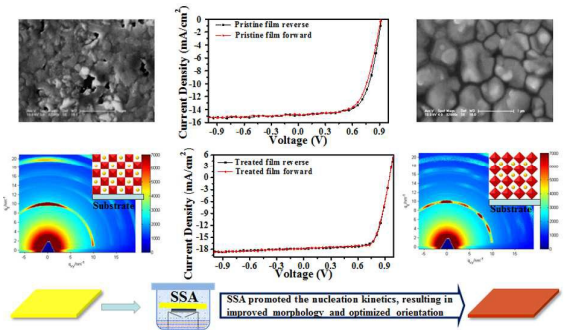

Here, perovskite nucleation process was controlled, producing films with optimized morphology and crystal orientation via the application of selective solvent annealing.